

Received July 12, 2018, accepted August 30, 2018, date of publication September 20, 2018, date of current version October 25, 2018.

Digital Object Identifier 10.1109/ACCESS.2018.2871618

# Modeling the Power Angular Profile of Dense Multipath Components Using Multiple Clusters

BRECHT HANSENS<sup>1</sup>, KENTARO SAITO<sup>2</sup>, (Member, IEEE),  
EMMERIC TANGHE<sup>1</sup>, (Member, IEEE), LUC MARTENS<sup>1</sup>, (Member, IEEE),  
WOUT JOSEPH<sup>1</sup>, (Senior Member, IEEE),  
AND JUN-ICHI TAKADA<sup>2</sup>, (Senior Member, IEEE)

<sup>1</sup>INTEC-WAVES, Ghent University-imec, 9052 Ghent, Belgium

<sup>2</sup>School of Environment and Society, Tokyo Institute of Technology, Tokyo 152-8550, Japan

Corresponding author: Emmeric Tanghe (emmeric.tanghe@ugent.be)

This work was supported in part by the FWO Project G027714N and the EOS project MULTi-Service Wireless NETWORK MUSE-WINET, in part by The Ministry of Internal Affairs and Communications through the Research and Development for Expansion of Radio Spectrum Resources, in part by JSPS KAKENHI under Grant 15H04003, in part by JSPS KAKENHI under Grant 16K18102, and in part by the Framework of COST Action CA15104 IRACON. The work of B. Hanssens was supported by the Agency for Innovation and Entrepreneurship through doctoral scholarship strategic Basic Research. E. Tanghe is a Post-Doctoral Fellow of the Research Foundation Flanders (FWO).

**ABSTRACT** In this paper, the power angular profile (PAP) of the dense multipath components (DMCs) was analyzed and characterized based on a channel sounding measurement campaign at 11 GHz in an indoor environment. The specular multipath components (SMCs) were estimated with the SAGE algorithm, and the RiMAX framework was applied for the estimation of the DMC in both the time-delay and the angular domain. After careful inspection of the spectrum of the residual signal components in the angular domain, we found that the DMC should be modeled by taking into account multiple angular clusters at different angles, to better characterize the diffuse scattering between transmitter and receiver, originating from multiple reflections in an environment. Therefore, we propose to extend the maximum likelihood estimation of the angular DMC parameters in the RiMAX framework so that the PAP of the DMC can be modeled with a multimodal von Mises distribution. We also validate our proposed method with the results of the measured channel sounding data.

**INDEX TERMS** Channel modeling, channel sounding, DMC, indoor, multipath estimation, polarization, RiMAX, SMC.

## I. INTRODUCTION

Over the recent years, mobile networks are becoming heavily congested due to the continuous increase in user traffic, caused by the emergence of wireless systems, mobile applications and streaming services. On top of that, the Internet of Things (IoT) is shifting from vision to reality. To accommodate for this additional demand in wireless signal spectrum, next-generation mobile communication systems such as 5G were developed, and are currently being investigated with increased interest [1], [2]. In the frequency bands utilized by 5G, massive Multiple-Input Multiple-Output (MIMO) technologies are expected to be employed to further enhance the data transmission capabilities of these systems, by relying on higher order beamforming and spatial multiplexing. The primary spectrum that is considered for the lower 5G bands all range between 1 GHz and 6 GHz, of which it is well known that their channel capacities are highly

influenced by the amount of diffuse scattering present in the radio channel. Diffuse scattering arises from radio waves scattering on electrically small and rough surfaces [3], which are inherently more present at sub-20 GHz frequencies in contrast to the higher 5G frequency bands (between 24 GHz and 30 GHz), mainly due to their shorter wavelengths and less attenuation. In indoor environments, where radio waves typically scatter from various objects, diffuse scattering plays an even more important role in the MIMO transmission capacity [4], [5]. However, its contribution is not taken into account in the standard channel models such as the 3GPP Spatial Channel Model (SCM) [6], the ITU-R M.2135 channel model [7], or the WINNER II channel model [8]. The aim of this paper is to gain more knowledge concerning an accurate and realistic angular modeling of diffuse scattering, and its effect on MIMO channel characteristics in lower frequency bands. The novelty is that we consider the existence

TABLE 1. Acronyms and symbols.

DMC	Dense Multipath Components
SMC	Specular Multipath Components
PAP	Power Angular Profile
PDP	Power Delay Profile
RSC	Residual Signal Components
$\mathbf{h}$	measured channel response vector
$\mathbf{s}(\theta_s)$	specular multipath components
$\mathbf{d}(\theta_d)$	dense multipath components
$\theta_s$	specular multipath parameters
$\theta_d$	dense multipath parameters
$\mathbf{r}$	residual signal components
$\varphi_T$	Angle of Departure (AoD)
$\varphi_R$	Angle of Arrival (AoA)
$\tau$	propagation time-delay
$\gamma$	complex amplitude per polarization state
$\mu_T$	Von Mises center parameter (AoD domain)
$\mu_R$	Von Mises center parameter (AoA domain)
$\kappa_T$	Von Mises concentration parameter (AoD domain)
$\kappa_R$	Von Mises concentration parameter (AoA domain)

of multiple angular clusters in the spectrum of the Residual Signal Components (RSC) of the radio channel, allowing us to construct a model that characterizes multiple reflections of the electromagnetic waves at different angles in the environment.

The structure of this paper is as follows. Section II summarizes the related work on this topic, whilst Section III describes the applied channel model with the angular modeling of the diffuse scattering. Section IV describes our methodology to apply this model to radio channel sounding data, and Section V presents the measurement campaign. Afterwards, Section VI describes the results of our approach. Finally, Section VII summarizes this paper with some conclusions and ideas for future work. Table 1 provides a list of oft-used acronyms and symbols required for a good understanding of the paper.

## II. RELATED WORK

Previous efforts to characterize the diffuse scattering mostly focused on measuring the far-field diffuse scattering pattern of typical building walls, and incorporating these results into diffuse scattering models for ray tracing simulators [9], [10]. Later works such as [11]–[13] utilized these models to extract information about the Power Delay Profile (PDP), the angular spread and the polarization characteristics of the diffuse scattering through ray tracing simulations, but the correctness of these analyses all relied on the accuracy with which the

environment was modeled in these simulators. In [14], the importance of correctly characterizing the DMC is emphasized to construct simple but realistic radio channel models.

More recent works such as [15]–[17] estimated the contributions of diffuse scattering directly from MIMO radio channel measurements by applying the RiMAX multipath estimation framework to estimate both the SMC and DMC from the measurement data. From a physical perspective, a radio channel is a collection of multipath components. Because channel sounders do not possess infinitely large apertures in the spatial and frequency domains, it is only possible to estimate the multipath components that stand out because of their Signal-to-Noise Ratio (SNR). These comprise the SMC: they give rise to constant phase relationships in the space, frequency, and time-delay domains which means that they can be coherently detected. On the other hand, the DMC are low-SNR multipath components that cannot be detected coherently due to the limitations of radio channel sounders: limited apertures prevent us from estimating dense multipath components individually, but we can describe their average power by means of continuous distributions. From a physical point of view, the SMC comprise the eventual line-of-sight component and the mirror-like interactions with objects in the environment (reflections, diffractions, and transmissions). The DMC originate mainly from diffuse scattering on electrically small and rough surfaces, but also contain low-SNR specular-like multipath components that cannot be resolved by the multipath estimator. The contributions of DMC are characterized by autocorrelations of the signal component, but the RiMAX framework only discusses the frequency domain correlation modeling of the DMC [15]–[18]. The integration of the DMC modeling in the angular domain into the RiMAX framework is often lacking in the literature.

In [19], a measurement campaign was performed in a large industrial hall in the 3 GHz band, of which the frequency domain DMC parameters were estimated for Line-of-Sight (LoS), Obstructed-LoS (OLOs) and Non-LoS (NLoS) scenarios. It was found that the fractional DMC power (i.e., relative to the total power) varies between 23%-38% in LoS, 27%-70% in OLOs, and 57%-64% in NLoS scenarios. Hence, it becomes evident that these DMC will contribute significantly to the total power in the channel at lower frequencies. In [20], this work was extended by measuring the polarization properties of the DMC in the same environment. Together with [21], which concerns an analysis of the DMC in the 4.5 GHz band, it was shown that the DMC parameters have a certain polarization dependency.

Investigations into the behavior of the angular DMC parameters found that correlations exist between the locations of the SMC and the dominating powers in the RSC spectrum. Therefore, [22] and [23] propose to model the DMC's angular profile as clusters around the SMC. In [24] and [25], a ML method is utilized based on a unimodal von Mises distribution to model the angular profile of the DMC. In [26], this distribution was also found to be a good fit to model

the angular domain autocorrelation function of the DMC in the 11 GHz band, by convolution of the angular DMC profile with the antenna array response. This work builds on the previous research on this topic [26], [27] by extending the conventional RiMAX framework from a unimodal- to a multimodal joint estimation of DMC propagation parameters in the frequency-, angular- and polarization domains. Since our proposed methodology outlined in Section IV was already validated by means of synthetic radio channel data based on Monte Carlo simulations [28], this paper presents the results based on channel sounding data of an indoor environment.

In this work, we will extend the ML method in the RiMAX algorithm from a unimodal- to a multimodal assumption, in order to account for multiple angular clusters in the DMC spectrum. We are able to model several angular clusters in the radio channel, originating from multiple reflections of the plane waves in an environment. Whereas the past literature focuses on sub-6 GHz frequency bands, this work sheds more light on the DMC characteristics in the X band through an 11 GHz MIMO measurement campaign [29] in an indoor environment. This paper extends our previous work on this topic [27], [30] by extending the conventional RiMAX framework for the joint estimation of multimodal DMC propagation parameters in the frequency, angular and polarization domains. We evaluated the benefits of adopting a multimodal angular distribution over a unimodal one, and have analyzed to which extent this will contribute to a better reconstruction of the eigenvalue structure of the MIMO channel. As was shown in [31] and [26], the DMC increases the level of the reconstructed eigenvalues, resulting in a better approximation of their measured values. This proves that an accurate modeling of the DMC parameters is necessary to prevent the underestimation of the MIMO transmission performance [5], and indicates the potential to increase the spectral efficiency of the radio communication link.

### III. CHANNEL MODEL

#### A. SPECULAR- AND DENSE MULTIPATH COMPONENTS

Multidimensional frequency domain channel sounding is a prerequisite in order to describe the geometric properties of the electromagnetic waves of the MIMO radio channel in terms of their characteristics in both the angular- and time-delay domain. This can be done with (virtual) MIMO antenna array systems, consisting of  $N_T$  and  $N_R$  antennas at transmitter (Tx) and receiver (Rx), sampled at  $N_F$  frequency points [32]. An observation of the MIMO radio channel  $\mathbf{h}$  can then be modeled as the superposition of SMC and DMC, and can be written as follows:

$$\mathbf{h} = \mathbf{s}(\boldsymbol{\theta}_s) + \mathbf{d}(\boldsymbol{\theta}_d), \quad (1)$$

in which  $\mathbf{h}$  can be seen as a random variable distributed according to a complex multivariate Gaussian distribution:

$$\mathbf{h} \sim \mathcal{N}_c(\mathbf{s}(\boldsymbol{\theta}_s), \mathbf{R}(\boldsymbol{\theta}_d)). \quad (2)$$

The SMC propagation parameter vector of the  $i$ -th path  $\boldsymbol{\theta}_{s,i}$  in the azimuthal plane consists of the angle-of-departure (AoD)

$\varphi_{T,i}$ , the azimuthal angle-of-arrival (AoA)  $\varphi_{R,i}$ , the propagation time-delay  $\tau_{s,i}$ , and the complex amplitude vector  $\boldsymbol{\gamma}_i = [\gamma_{s,vv,i}, \gamma_{s,vh,i}, \gamma_{s,hv,i}, \gamma_{s,hh,i}]$ . In the adopted signal model, the SMC of the  $i$ -th path  $\mathbf{s}(\boldsymbol{\theta}_{s,i}) \in \mathbb{C}^{N_T N_R N_F \times 1}$  is defined as follows:

$$\boldsymbol{\theta}_{s,i} = [\varphi_{T,i}, \varphi_{R,i}, \tau_{s,i}, \boldsymbol{\gamma}_i], \quad (3)$$

$$\mathbf{s}(\boldsymbol{\theta}_{s,i}) = \boldsymbol{\alpha}_T(\varphi_{T,i}) \otimes \boldsymbol{\alpha}_R(\varphi_{R,i}) \otimes \boldsymbol{\alpha}_F(\tau_{s,i}) \boldsymbol{\gamma}_i. \quad (4)$$

In (4),  $\boldsymbol{\alpha}_T$  and  $\boldsymbol{\alpha}_R$  are the antenna array responses of the Tx and Rx, respectively, and  $\boldsymbol{\alpha}_F(\tau_{s,i})$  is the frequency transfer function of the impulse response  $\delta(\tau - \tau_{s,i})$ . The  $\otimes$  symbol represents the Kronecker product.

The DMC is modeled stochastically by means of the covariance matrix of the RSC part of the radio channel  $\mathbf{R}(\boldsymbol{\theta}_d)$ , based on the DMC propagation parameters  $\boldsymbol{\theta}_{d,F}$  in the frequency domain, and  $\boldsymbol{\theta}_{d,A}$  in the angular-polarization domain, defined as follows:

$$\boldsymbol{\theta}_{d,F} = [\alpha_0, \alpha_1, \beta_d, \tau_d], \quad (5)$$

$$\boldsymbol{\theta}_{d,A} = [\mu_T, \mu_R, \kappa_R, \kappa_R, \gamma_{d,vv}, \gamma_{d,vh}, \gamma_{d,hv}, \gamma_{d,hh}, \gamma_\alpha]. \quad (6)$$

In [15] and [16], the PDP of the DMC in the time-delay domain is modeled based on the observation that its power  $f_F(\tau)$  has a base delay  $\tau_d$  related to the distance between Tx and Rx, with an exponential decay over time-delay (see Eq. (7)), corrupted by complex additive white Gaussian noise with power  $\alpha_0$ :

$$f_F(\tau) = \begin{cases} \alpha_1 e^{-B_d(\tau - \tau_d)} + \alpha_0, & \text{if } \tau > \tau_d \\ \alpha_0, & \text{otherwise.} \end{cases} \quad (7)$$

The DMC and noise power spectrum density  $\kappa(\boldsymbol{\theta}_{d,F})$  in the frequency domain denotes a sampled version of  $f_F(\tau)$  in Eq. (7) under the finite bandwidth condition, and is defined as follows:

$$\kappa(\boldsymbol{\theta}_{d,F}) = \frac{\alpha_1}{N_F} \left[ \frac{1}{\beta_d}, \frac{e^{-j2\pi\tau_d}}{\beta_d + \frac{j2\pi}{N_F}} \dots \frac{e^{-j2\pi(N_F-1)\tau_d}}{\beta_d + \frac{j2\pi(N_F-1)}{N_F}} \right] + \alpha_0 \mathbf{e}_0. \quad (8)$$

In Eq. (8),  $\mathbf{e}_0 = [1, 0, \dots, 0]$  is a unit vector, and  $\beta_d = B_d/B_m$  is the coherent bandwidth, which is normalized by the measurement bandwidth  $B_m$ . Then, the frequency domain correlation matrix  $\mathbf{R}_F(\boldsymbol{\theta}_{d,F}) \in \mathbb{C}^{N_F \times N_F}$  of the diffuse scattering can be calculated by applying the Toeplitz-operator [15] as follows:

$$\mathbf{R}_F(\boldsymbol{\theta}_{d,F}) = \text{toep} \left( \kappa(\boldsymbol{\theta}_{d,F}), \kappa^H(\boldsymbol{\theta}_{d,F}) \right). \quad (9)$$

#### B. MULTIMODAL ASSUMPTION OF DMC IN ANGULAR DOMAIN

In [24], [33], and [34], the Power Angular Profile (PAP) of the DMC at Tx or Rx in the azimuth plane is modeled using a unimodal von Mises distribution, which is defined (e.g., at Tx) as follows:

$$f_T(\varphi) = \frac{1}{2\pi I_0(\kappa_T)} \exp(\kappa_T \cos(\varphi - \mu_T)), \quad (10)$$

with  $I_0(\kappa_T)$  being the modified Bessel function of the first kind and zeroth order, the parameter  $\mu_T$  controlling the center location of the distribution at Tx, and  $\kappa_T$  controlling its angular spread. As the value for  $\kappa_T$  increases, the angular spread of the distribution decreases, and the distribution gets narrower. For larger values of  $\kappa$ , the von Mises distribution approaches the normal distribution. For a  $\kappa$  value of 0, the von Mises distribution approaches the uniform distribution, meaning that the diffuse power is equal throughout the angular RSC spectrum, regardless of at which angle we observe this diffuse power. This model for the PAP of the DMC can be regarded as the most likely fit of the measured RSC in the angular domain.

In the polarimetric scenario, the PAP is modeled by multiplying the von Mises distribution with an angle-independent polarization vector  $\boldsymbol{\gamma}_d = [\gamma_{d,vv}, \gamma_{d,vh}, \gamma_{d,hv}, \gamma_{d,hh}, \gamma_\alpha]$  [25]. The angular and polarization domain covariance matrix  $\mathbf{R}_A(\boldsymbol{\theta}_{d,A}) \in \mathbb{C}^{N_T N_R \times N_T N_R}$  can then be written as follows:

$$\mathbf{R}_A(\boldsymbol{\theta}_{d,A}) = \mathbf{R}_{vv} + \mathbf{R}_{vh} + \mathbf{R}_{hv} + \mathbf{R}_{hh} + \gamma_\alpha \mathbf{I}. \quad (11)$$

In Eq. (11),  $\gamma_\alpha$  denotes the noise power in the angular domain.

In the multimodal assumption of the angular DMC power spectrum, multiple clusters exists in the PAP of Tx and Rx, each with their own von Mises distribution defined by a center location  $\mu$  and an angular spread  $\kappa$ . We can write the angular domain covariance matrix  $\mathbf{R}_{xy}$  for a certain polarization setting  $xy$  (e.g., Tx-V and Rx-H; denoted as VH) as being the summation over several separate covariance matrices, which can be written as follows:

$$\mathbf{R}_{xy} = \sum_{c_t=1}^{C_T} \sum_{c_r=1}^{C_R} \gamma_{d,xy}^{c_t, c_r} \mathbf{C}_{xy}^{c_t, c_r}, \quad (12)$$

with  $C_T$  and  $C_R$  the number of clusters in the PAP of Tx and Rx, respectively. In Eq. (12),  $\mathbf{C}_{xy}^{c_t, c_r}$  is the combined Tx and Rx angular power spectrum, and can be written as the Kronecker-product between both  $\mathbf{C}_x^{c_t}$  and  $\mathbf{C}_y^{c_r}$  (their separate angular power spectrum) as follows:

$$\mathbf{C}_{xy}^{c_t, c_r} = \mathbf{C}_x^{c_t} \otimes \mathbf{C}_y^{c_r} \quad (13)$$

$$\mathbf{C}_x^{c_t} = \int_{-\pi}^{\pi} \boldsymbol{\alpha}_{T,x}(\varphi) f_T^{c_t}(\varphi) \boldsymbol{\alpha}_{T,x}^H(\varphi) d\varphi \quad (14)$$

$$\mathbf{C}_y^{c_r} = \int_{-\pi}^{\pi} \boldsymbol{\alpha}_{R,y}(\varphi) f_R^{c_r}(\varphi) \boldsymbol{\alpha}_{R,y}^H(\varphi) d\varphi, \quad (15)$$

in which  $f_T^{c_t}(\varphi)$  and  $f_R^{c_r}(\varphi)$  are both unimodal von Mises distributions of the  $c_t$ -th cluster at Tx, and the  $c_r$ -th cluster at Rx, respectively. In (14) and (15),  $\boldsymbol{\alpha}_{T,x}$  and  $\boldsymbol{\alpha}_{R,y}$  are the antenna array responses of the transmitter for the polarization setting  $x$ , and the receiver for the polarization setting  $y$ , respectively. The combined PAP at Tx and Rx will consist of a multitude of angular clusters, so that the DMC angular parameters of multiple reflections at different angles in the environment can be better characterized. As we will show in Section VI, this results in a better reconstruction of the eigenvalue structure of the MIMO channel.

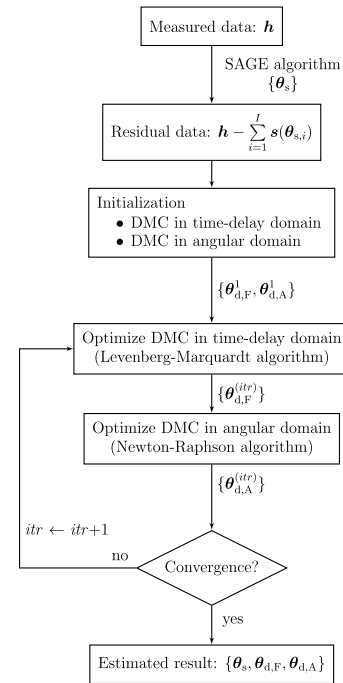


FIGURE 1. RiMAX multipath estimator.

Finally, the full DMC correlation matrix  $\mathbf{R}$  is calculated as follows:

$$\mathbf{R} = \mathbf{R}_F(\boldsymbol{\theta}_{d,F}) \otimes \mathbf{R}_A(\boldsymbol{\theta}_{d,A}). \quad (16)$$

However, since the aim of this work is to model the spatial (angular) properties of the DMC, we will omit the frequency domain from the covariance matrix, as was done before in [25]. We will model  $\mathbf{R}_F(\boldsymbol{\theta}_{d,F})$  as a unitary matrix.

#### IV. METHODOLOGY

Figure 1 presents a flowchart of our version of the RiMAX multipath estimator. This framework is used to obtain estimates of the SMC and DMC parameters defined in the channel model of Section III.

Regarding the SMC, the SMC parameter vector  $\boldsymbol{\theta}_{s,i}$  is estimated from the measurement data  $\mathbf{h}$  using the SAGE algorithm [35]. Subsequently, the estimated SMC are subtracted from the measured channel so that only the DMC remains in the residual data. Next, the time-delay and angular-polarization domain propagation parameters of the DMC are initialized and sequentially optimized with either the Levenberg-Marquardt or the Newton-Raphson method. The log-likelihood function of the DMC can be calculated by using the correlation matrix  $\tilde{\mathbf{R}}$  of the RSC spectrum  $\mathbf{r}$  after removal of all the SMC from the measured data, which are both defined as follows:

$$\mathbf{r} = \mathbf{h} - \sum_{i=1}^I s(\boldsymbol{\theta}_{s,i}) \quad (17)$$

$$\tilde{\mathbf{R}} = \mathbf{r} \mathbf{r}^H, \quad (18)$$

so that we can write the log-likelihood function as follows:

$$\mathcal{L}(\mathbf{h}|\boldsymbol{\theta}_{d,F}, \boldsymbol{\theta}_{d,A}) = -\ln(\det(\mathbf{R})) - \text{tr}(\mathbf{R}^{-1}\tilde{\mathbf{R}}) + C, \quad (19)$$

in which  $C$  is a constant.

The DMC propagation parameters  $\boldsymbol{\theta}_{d,F}$  in the time-delay domain, and  $\boldsymbol{\theta}_{d,A}$  in the angular-polarization domain are estimated separately in order to reduce the computational complexity of performing a multidimensional search for the joint maximization of this log-likelihood function. We will try to maximize this objective function by alternating between the optimization procedures with respect to the parameter subsets  $\boldsymbol{\theta}_{d,F}$  and  $\boldsymbol{\theta}_{d,A}$ . For the estimation of  $\boldsymbol{\theta}_{d,F}$  in the time-delay domain, the angular-polarization domain of the RSC spectrum is first shrunk by the estimation result of  $\mathbf{R}_A(\boldsymbol{\theta}_{d,A}^{(itr)})$  of the previous iteration, calculated as follows:

$$\mathbf{d}_F = \text{mat}\{\mathbf{d}, N_F, N_T N_R\} \mathbf{L}_A \quad (20)$$

$$\tilde{\mathbf{R}}_F = \frac{1}{N_T N_R} \mathbf{d}_F \mathbf{d}_F^H, \quad (21)$$

in which  $\text{mat}\{A, m, n\}$  is a matrix operator that reshapes a vector  $A$  into an  $m \times n$  matrix, and  $\mathbf{L}_A$  is the matrix satisfying  $\mathbf{L}_A \mathbf{L}_A^H = \mathbf{R}_A(\boldsymbol{\theta}_{d,A}^{(itr)})^{-1}$ . The time-delay and angular-polarization domain log-likelihood functions can be written as follows:

$$\begin{aligned} \mathcal{L}_F(\mathbf{h}|\boldsymbol{\theta}_{d,F}) &= -\ln(\det(\mathbf{R}_F(\boldsymbol{\theta}_{d,F}))) \\ &\quad - \text{tr}(\mathbf{R}_F(\boldsymbol{\theta}_{d,F})^{-1} \tilde{\mathbf{R}}_F) + C' \end{aligned} \quad (22)$$

$$\begin{aligned} \mathcal{L}_A(\mathbf{h}|\boldsymbol{\theta}_{d,A}) &= -\ln(\det(\mathbf{R}_A(\boldsymbol{\theta}_{d,A}))) \\ &\quad - \text{tr}(\mathbf{R}_A(\boldsymbol{\theta}_{d,A})^{-1} \tilde{\mathbf{R}}_A) + C'', \end{aligned} \quad (23)$$

in which  $C'$  and  $C''$  are constants.

### A. INITIALIZATION OF DMC PROPAGATION PARAMETERS

To find a suitable final solution for both the time-delay and the angular-polarization domain DMC parameters described above, we must first start the iterative search from an initial solution. Since we have adopted the same method of [15] for finding an initial solution for the time-delay domain DMC parameters, we refer to this work for a detailed description.

For the initialization of the angular-polarization DMC parameters, we need to know how many clusters (i.e., distributions) to consider at Tx and Rx, what their center values are, their angular spreads, and the polarimetric power they represent in the RSC spectrum. The initialization of each of these four characteristics will be discussed in the section below.

In a first step towards the initialization of the angular-polarization domain DMC parameters, the estimated SMC values of the AoD and AoA per propagation path are fed as input parameters to a k-means clustering algorithm [36]. It should be noted that we perform this clustering separately at the transmitter and receiver, so that we can obtain a different number of clusters at the transmitter and receiver. The k-means algorithm (e.g., at transmitter) aims to partition the  $I$  different AoD values of the SMC into a certain pre-defined number of clusters  $k$  in which each angle belongs

to the cluster with the nearest mean. K-means clustering aims to partition these  $I$  AoD values into  $k$  sets ( $k \leq I$ ), so as to minimize the within-cluster sum of squares (WCSS) (i.e., the variance). This is the equivalent of minimizing the pairwise squared deviations between the AoDs in the same cluster. Because the total variance is constant, this is also equivalent to maximizing the squared deviations between the AoDs in different clusters (between-cluster sum of squares, BCSS). The k-means algorithm was run 200 times for each measured radio channel matrix and each value of  $k$ , each time with different random initial values for the cluster centroids. Of those 200 executions, only the clustering result with the smallest WCSS summed over the  $k$  clusters was retained.

The result of this algorithm is in agreement with the definition of a cluster in the COST 273 and COST 2100 channel models, namely that a cluster is a set of propagation paths with similar characteristics [37], [38]. By running the k-means algorithm for a varying number of clusters which are to be formed (e.g., 2 to 5), the optimal number of clusters can be estimated by using the Kim-Parks (KP) clustering index [39]. This KP index employs two partition functions showing opposite properties around the optimal number of clusters. The Kim-Parks index is preferred over other more common validity indices that make use of intra-cluster and inter-cluster separation measures, as these indices tend to decrease or increase monotonically with the number of clusters. The Kim-Parks index circumvents this behavior by normalizing the index by the index values at the minimum and maximum number of clusters. Note that modeling a single cluster could be better in some scenarios (e.g., for an open outdoor environment without much reflection). To detect such a situation, we will check during the optimization procedure if the angular spread of a certain cluster is still significantly large (i.e.,  $\kappa \leq 0.05$ ). If not, this cluster will act as a uniform distribution in angular space, and it has no added value to model the diffuse powers in the angular RSC spectrum. We will drop this cluster from further analysis in the algorithm.

In our approach, we will limit the maximum number of clusters to 3, so that we do not overfit the angular RSC spectrum, and also reduce the computational complexity of finding an optimal set of values for them. We will take the center values of each k-means-classified cluster  $c_t$  at Tx (i.e., the clustered AoD values) as center values  $\mu_T^{c_t}$  for each distribution  $f_T^{c_t}$ . Similarly, the center values of each k-means-classified cluster  $c_r$  at Rx (i.e., the clustered AoA values) will act as the center values  $\mu_R^{c_r}$  for each distribution  $f_R^{c_r}$ .

After doing so, we will use these initialized center values  $\mu$  of the von Mises distributions, and apply a beamforming based method with a coarse grid search for the initialization of their respective  $\kappa$  values. First, we need to write the total angle-independent polarimetric power vector  $\boldsymbol{\zeta}_d^{c_t, c_r}$ , representing the polarimetric power between the angular DMC clusters  $c_t$  at Tx, and  $c_r$  at Rx, as follows:

$$\boldsymbol{\zeta}_d^{c_t, c_r} = \text{vec} \left\{ \left[ \zeta_{d,vv}^{c_t, c_r}, \zeta_{d,vh}^{c_t, c_r}, \zeta_{d,hv}^{c_t, c_r}, \zeta_{d,hh}^{c_t, c_r} \right] \right\}, \quad (24)$$

in which  $\text{vec}\{\cdot\}$  is an operator that reshapes a matrix into a row vector. We can then construct a model from Eq. (11), relying on the linear dependences of the covariance matrix  $\mathbf{R}_A$  as follows:

$$\mathbf{R}_{A,v} = \text{vec}\{\mathbf{R}_A\} \quad (25)$$

$$\mathbf{R}_{A,v} = \sum_{c_t=1}^{C_T} \sum_{c_r=1}^{C_R} \zeta_d^{c_t, c_r} \mathbf{C}_d^{c_t, c_r} + \zeta_\alpha \text{vec}\{\mathbf{I}\} \quad (26)$$

$$\mathbf{C}_d^{c_t, c_r} = \begin{bmatrix} \text{vec}\{\mathbf{C}_{vv}^{c_t, c_r}\} \\ \text{vec}\{\mathbf{C}_{vh}^{c_t, c_r}\} \\ \text{vec}\{\mathbf{C}_{hv}^{c_t, c_r}\} \\ \text{vec}\{\mathbf{C}_{hh}^{c_t, c_r}\} \end{bmatrix}, \quad (27)$$

which we can rewrite as follows:

$$\mathbf{R}_{A,v} = \zeta_v \mathbf{C}_v \quad (28)$$

$$\zeta_v = \text{vec} \left\{ \left[ \zeta_d^{1,1}, \zeta_d^{1,2}, \dots, \zeta_d^{1,C_R}, \dots, \zeta_d^{C_T,1}, \zeta_d^{C_T,2}, \dots, \zeta_d^{C_T,C_R}, \zeta_\alpha \right] \right\} \quad (29)$$

$$\mathbf{C}_v = \text{vec} \left\{ \left[ \mathbf{C}_d^{1,1}, \mathbf{C}_d^{1,2}, \dots, \mathbf{C}_d^{1,C_R}, \dots, \mathbf{C}_d^{C_T,1}, \mathbf{C}_d^{C_T,2}, \dots, \mathbf{C}_d^{C_T,C_R}, \mathbf{I} \right]^T \right\}. \quad (30)$$

Exploiting this linear model, we can apply a Minimum Mean Square Error (MMSE) estimator that minimizes the mean square error between the sample covariance matrix and the model covariance matrix as follows [40], [41]:

$$\hat{\zeta}_v = \min_{\zeta_v} \left\| \tilde{\mathbf{R}}_{A,v} - \zeta_v \mathbf{C}_v \right\|^2, \quad (31)$$

from which we can calculate that the optimal value  $\hat{\zeta}_v$  according to the MMSE estimator becomes the following:

$$\hat{\zeta}_v = \tilde{\mathbf{R}}_{A,v} \left( \left( \mathbf{C}_v^* \mathbf{C}_v^T \right)^{-1} \mathbf{C}_v^* \right)^T, \quad (32)$$

from which we can calculate the covariance matrix in the angular domain  $\mathbf{R}_A(\boldsymbol{\theta}_{d,A})$ , and insert it into the log-likelihood function of the angular-polarization domain of the RiMAX algorithm (see Eq. (23)). The optimal (coarsely searched)  $\kappa$  values, resulting in the highest value of this log-likelihood function among all initial values, will be used as initial starting values in a next iteration of this beamforming search, around which we will choose finer  $\kappa$  values. After doing so, we can find a set of finely searched  $\kappa$  values which best represent the angular-polarization profile of the RSC spectrum. The angle-independent polarization matrix  $\zeta_v$ , representing the polarimetric power corresponding between the Tx and Rx angular DMC clusters, can be calculated from Eq. (32).

## B. OPTIMIZATION OF DMC PROPAGATION PARAMETERS

### 1) TIME-DELAY DOMAIN DMC OPTIMIZATION

To optimize the time-delay domain DMC parameters, we will make use of the Levenberg-Marquardt algorithm in the frequency domain for the optimization of the DMC propagation parameter  $\boldsymbol{\theta}_{d,F}$  [15]. Firstly, the Jacobian  $\mathbf{D}_F(\boldsymbol{\theta}_{d,F}^{(itr)})$  of the

frequency domain log-likelihood function  $\mathcal{L}_F(\mathbf{h}|\boldsymbol{\theta}_{d,F})$  needs to be calculated as follows:

$$\mathbf{D}_F(\boldsymbol{\theta}_{d,F}^{(itr)}) = \text{diag} \left\{ \Gamma_C \left\{ \kappa(\boldsymbol{\theta}_{d,F}^{(itr)}) \right\} \right\}^{-1} \times \left[ \Gamma_C \left\{ \frac{\partial \kappa(\boldsymbol{\theta}_{d,F})}{\partial \theta_{d,F,1}} \right\}, \dots, \Gamma_C \left\{ \frac{\partial \kappa(\boldsymbol{\theta}_{d,F})}{\partial \theta_{d,F,4}} \right\} \right], \quad (33)$$

in which  $\Gamma_C \{\cdot\}$  is the smoothing operator as defined in [15]. The propagation parameter  $\boldsymbol{\theta}_{d,F}^{(itr)}$  is then updated by the incremental step  $\Delta \boldsymbol{\theta}_{d,F}^{(itr)}$  to minimize the residual error  $\epsilon^{(itr)}$  as follows:

$$\epsilon^{(itr)} = \text{diag} \left\{ \Gamma_C \left\{ \kappa(\boldsymbol{\theta}_{d,F}^{(itr)}) \right\} \right\}^{-1} \Gamma_C \{\mathbf{d}_F\} - 1 \quad (34)$$

$$\Delta \boldsymbol{\theta}_{d,F}^{(itr)} = \left( \mathbf{D}_F^T \mathbf{D}_F + \lambda_F \mathbf{I} \cdot \mathbf{D}_F^T \mathbf{D}_F \right)^{-1} \mathbf{D}_F^T \epsilon^{(itr)} \quad (35)$$

$$\boldsymbol{\theta}_{d,F}^{(itr+1)} = \boldsymbol{\theta}_{d,F}^{(itr)} + \Delta \boldsymbol{\theta}_{d,F}^{(itr)}, \quad (36)$$

in which  $\lambda_F$  is the step length, initialized at 1. If the resulting updated parameter  $\boldsymbol{\theta}_{d,F}^{(itr+1)}$  causes an increase in the log-likelihood function Eq. (22), convergence is achieved,  $\lambda_F$  is divided by 2, and we will start the optimization of the angular-polarization DMC propagation parameter. If not,  $\lambda_F$  is multiplied by 4, and the algorithm keeps searching for a new updated parameter  $\boldsymbol{\theta}_{d,F}^{(itr+1)}$  until convergence is achieved. It should be noted that the division by 2 and multiplication by 4 were arbitrary choices, and other values could result in a faster convergence of the algorithm.

### 2) ANGULAR-POLARIZATION DOMAIN DMC OPTIMIZATION

After the optimization of the time-delay DMC propagation parameter  $\boldsymbol{\theta}_{d,F}$ , the angular-polarization domain DMC propagation parameter  $\boldsymbol{\theta}_{d,A}$  will be optimized by making use of the Newton-Raphson algorithm [25]. Firstly, the score function  $\mathbf{q}_A(\mathbf{h}|\boldsymbol{\theta}_{d,A})$  and the Fisher information matrix  $\mathbf{J}_A(\boldsymbol{\theta}_{d,A})$  of the angular-polarization domain log-likelihood function  $\mathcal{L}_A(\mathbf{h}|\boldsymbol{\theta}_{d,A})$  need to be calculated as follows:

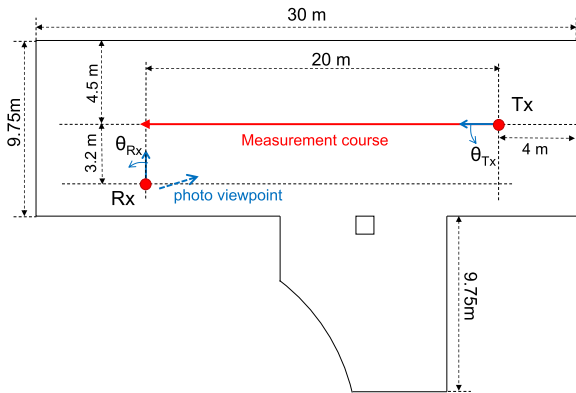
$$\mathbf{q}_A(\mathbf{h}|\boldsymbol{\theta}_{d,A}) = \text{tr} \left( \mathbf{R}_A(\boldsymbol{\theta}_{d,A}^{(itr)})^{-1} \left[ \frac{\partial \mathbf{R}_A(\boldsymbol{\theta}_{d,A}^{(itr)})}{\partial \boldsymbol{\theta}_{d,A}} \right] \mathbf{R}_A(\boldsymbol{\theta}_{d,A}^{(itr)})^{-1} \tilde{\mathbf{R}}_A - \mathbf{I} \right) \quad (37)$$

$$\mathbf{J}_A(\boldsymbol{\theta}_{d,A})_{ij} = \text{tr} \left( \mathbf{R}_A(\boldsymbol{\theta}_{d,A}^{(itr)})^{-1} \frac{\partial \mathbf{R}_A(\boldsymbol{\theta}_{d,A}^{(itr)})}{\partial \theta_{d,A,i}} \mathbf{R}_A(\boldsymbol{\theta}_{d,A}^{(itr)})^{-1} \frac{\partial \mathbf{R}_A(\boldsymbol{\theta}_{d,A}^{(itr)})}{\partial \theta_{d,A,j}} \right). \quad (38)$$

The propagation parameter  $\boldsymbol{\theta}_{d,A}^{(itr)}$  is then updated by the incremental step  $\Delta \boldsymbol{\theta}_{d,A}^{(itr)}$  as follows:

$$\Delta \boldsymbol{\theta}_{d,A}^{(itr)} = -\mathbf{J}_A(\boldsymbol{\theta}_{d,A}^{(itr)})^{-1} \mathbf{q}_A(\mathbf{h}|\boldsymbol{\theta}_{d,A}^{(itr)}) \quad (39)$$

$$\boldsymbol{\theta}_{d,A}^{(itr+1)} = \boldsymbol{\theta}_{d,A}^{(itr)} + \lambda_A \Delta \boldsymbol{\theta}_{d,A}^{(itr)}, \quad (40)$$



(a)



(b)

**FIGURE 2.** Measurement environment [26]. (a) Floor plan. (b) Photograph.

in which  $\lambda_A$  is the step length, initialized at 1. If the resulting updated parameter  $\theta_{d,A}^{(itr+1)}$  causes an increase in the log-likelihood function Eq. (23), convergence is achieved, and we will start the next iteration with the optimization of the time-delay DMC propagation parameter. If not,  $\lambda_A$  is divided by 4, and the algorithm keeps searching for a new updated parameter  $\theta_{d,A}^{(itr+1)}$  until convergence is achieved.

## V. MEASUREMENTS

### A. MEASUREMENT ENVIRONMENT

Figure 2 shows the measurement environment of the indoor hall, with a description of the floor plan in Figure 2a, and a photograph of it from the viewpoint of the receiver in Figure 2b.

Figure 2a shows that there was no furniture in this environment, except for a few chairs and some tables. This size of the hall was approximately 30 m  $\times$  10 m  $\times$  3 m. In this environment, the receiver was set at a fixed position (bottom left in Figure 2a), whilst the transmitter occupied various positions along the measurement course (starting from center right in Figure 2a, going to center left). In total, 280 distinct transmitter-receiver locations were measured along the 20 m course, resulting in a spacing between the measurement

**TABLE 2.** Channel sounder parameters.

Center frequency	11 GHz
Bandwidth	400 MHz
Transmit power (per antenna)	10 mW
Transmit signal	Multitone signal
Number of sub-carriers	2048
Tx/Rx antenna array	12-element circular array (12 V-pol. and 12 H-pol.)
Tx/Rx antenna height	1.7 m

points of about 7.17 cm. Snapshot 0 was located at the utmost right of ‘measurement course’ in Figure 2a, whilst snapshot 279 was located at the utmost left in this course. The array directions of transmitter are also shown, and the AoD and AoA were defined from the front directions of the instruments in a counter-clockwise direction (see Figure 2a).

In the data analysis, the SMC parameters were first estimated with the SAGE algorithm [35]. The path discarding threshold  $\xi$  was 20 dB, such that paths with a lower power than the highest path power by  $\xi$  were discarded. In total, we allowed for the estimation of a maximum number of 90 propagation paths. Afterwards, the angular-polarization characteristics of the DMC propagation parameters were estimated with the RiMAX-based estimator that was explained in Section IV. In our analysis, we will compare the characteristics of assuming a uniform-, unimodal- and multimodal angular DMC assumption. The data processing parameters are summarized in Table 3.

### B. CHANNEL SOUNDING CAMPAIGN

MIMO channel measurements were conducted in the 11 GHz band in an indoor hall environment to identify the angular-polarization characteristics of the DMC in the X band. The specifications of the MIMO channel sounder are summarized in [29], and its main settings are listed in Table 2. The antennas were dual-polarized patch antennas, so that the 12-element circular array at transmitter and receiver gives rise to a 24-by-24 MIMO channel matrix (12 H-polarized channels and 12 V-polarized channels). A photographs of the 11 GHz channel sounder with transmitter- and receiver unit is shown in Figure 3.

## VI. RESULTS

### A. MEASURED ANGULAR SPECTRA

Figures 4a and 4b show the measured RSC power spectrum and its estimated PAPs for snapshot 140 at Tx and Rx, respectively. At both the transmitter and the receiver, our methodology resulted in the estimation of two clusters. In these figures, the black line represents the RSC power spectrum in the angular domain, summed over all time-delay bins.



FIGURE 3. Photograph of the 11 GHz channel sounder.

TABLE 3. Data processing parameters.

Maximum number of paths	90
SAGE: maximum iteration number	20
RiMAX: maximum iteration number	100
Path discarding threshold $\xi$	20 dB

To obtain this angular spectrum, e.g. at Tx, we first perform the following beamforming operation [42]:

$$S_T(\varphi_T) = \frac{1}{N_R} \sum_{n_R=1}^{N_R} \frac{\mathbf{B}_T(\varphi_T)^H}{\sqrt{\mathbf{B}_T(\varphi_T)^H \mathbf{B}_T(\varphi_T)}} \mathbf{Y}_{n_R}, \quad (41)$$

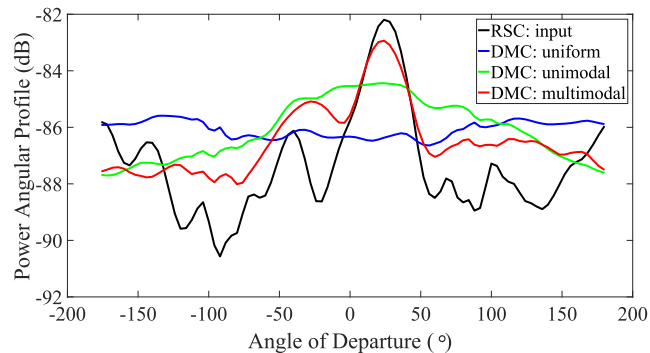
in which  $\mathbf{Y}_{n_R} \in \mathbb{C}^{N_T \times N_F}$  denotes the impulse response of all Tx channels and the  $n_R^{\text{th}}$  Rx channel for the residual channel  $\mathbf{r}$  (i.e., measured minus SMC), and  $\mathbf{B}_T(\varphi_T)$  denotes the antenna array responses of the transmitter for the angle  $\varphi_T$ . Equivalently, the angular spectrum of the RSC at Rx is calculated as follows:

$$S_R(\varphi_R) = \frac{1}{N_T} \sum_{n_T=1}^{N_T} \frac{\mathbf{B}_R(\varphi_R)^H}{\sqrt{\mathbf{B}_R(\varphi_R)^H \mathbf{B}_R(\varphi_R)}} \mathbf{Y}_{n_T}, \quad (42)$$

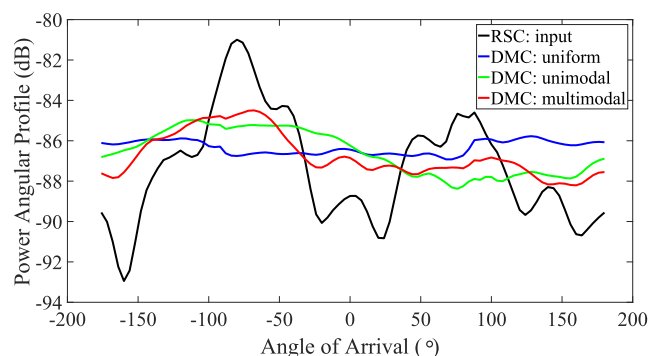
in which  $\mathbf{Y}_{n_T} \in \mathbb{C}^{N_R \times N_F}$  denotes the impulse response of all Rx channels and the  $n_T^{\text{th}}$  Tx channel for the residual channel  $\mathbf{r}$ , and  $\mathbf{B}_R(\varphi_R)$  denotes the antenna array responses of the receiver for the angle  $\varphi_R$ . Afterwards, an Inverse Fast Fourier Transform (IFFT) operation is performed to get the time-delay domain representation of these angular spectra, after which we sum them over all time-delay bins.

In Figure 4, the red line corresponds with the PAPs of the multimodal DMC assumption, whilst the green line is the PAP of the unimodal DMC assumption, and the blue line represents a uniform angular distribution of power. Figure 4a is the RSC power spectrum at the transmitter, and figure 4b is the RSC power spectrum at the receiver.

Figure 4a and 4b show that the multimodal angular DMC assumption is a better representation of the RSC spectrum



(a)



(b)

FIGURE 4. PAPs of the measured RSC spectrum and the reconstructed DMC spectra assuming a uniform-, unimodal- and multimodal assumption for snapshot 140. (a) Transmitter. (b) Receiver.

than the unimodal- or the uniform angular DMC assumption. Figure 4b clearly shows that the center locations of the multimodal distribution are estimated better with the multimodal assumption over the unimodal one, and lie closer to the peak values in the angular RSC spectrum. However, there is still room for improvement regarding the extent to which the angular RSC spectrum can be reconstructed, which is largely influenced by the amount of variation in this spectrum.

### B. MEAN-SQUARE-ERRORS OF THE RSC CHARACTERIZATION

Figure 5 presents the Mean-Square-Errors (MSEs) between the RSC and its reconstructed spectrum using the uniform-, unimodal- and multimodal angular DMC assumptions for the 280 distinct Tx-Rx positions, shown as a function of their traveled length along the measurement route (0 m to 20 m).

Figure 5 visually shows that the MSE between the RSC and the different angular DMC assumption significantly lowers when going from a uniform- to a unimodal- to a multimodal angular DMC assumption. Table 4 lists the MSE between the RSC and these three angular DMC assumptions using either the total angular RSC spectrum, or the 95% strongest values in it.

Table 4 shows that the MSE between the RSC and the reconstructed spectrum assuming a uniform angular distribution is about 7.65 dB at the transmitter, and 7.49 dB at

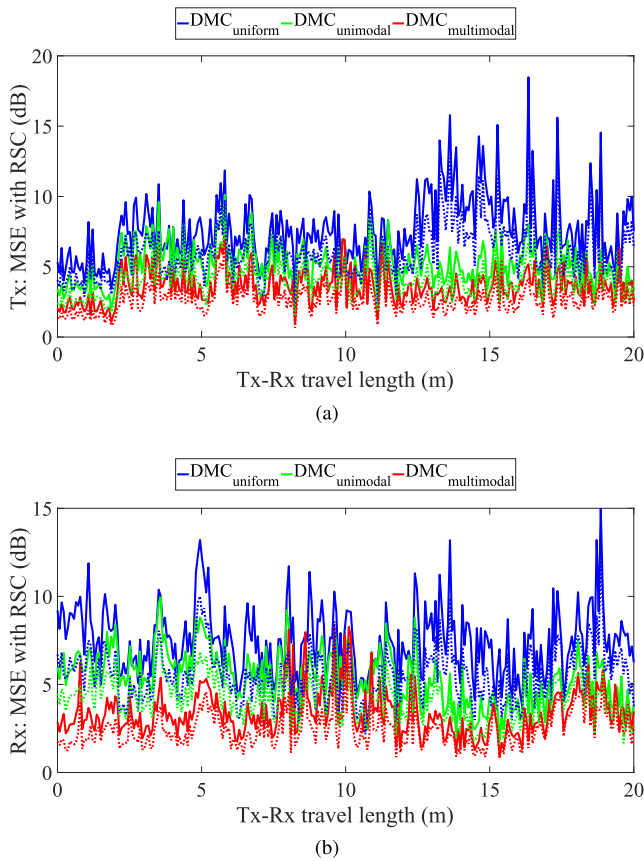


FIGURE 5. MSE of the angular RSC spectrum with its reconstructed spectrum using a uniform- (blue), unimodal- (green), or multimodal (red) angular DMC assumption. (a) Transmitter. (b) Receiver.

TABLE 4. MSEs between the RSC and the uniform-, unimodal- and multimodal angular DMC assumptions for the total angular RSC spectrum and the 95% strongest values in it.

		uniform	unimodal	multimodal
Tx	total spectrum	7.65 dB	5.20 dB	3.57 dB
	95% strongest	6.06 dB	3.98 dB	2.65 dB
Rx	total spectrum	7.49 dB	5.49 dB	3.38 dB
	95% strongest	5.55 dB	4.17 dB	2.49 dB

the receiver. When applying a unimodal angular DMC distribution, this error reduces to 5.20 dB at the transmitter, and 5.49 dB at the receiver. Moreover, when we apply a multimodal angular DMC distribution, this error reduces even further to 3.57 dB at the transmitter, and 3.38 dB at the receiver. Looking at this MSE, the multimodal angular DMC distribution outperforms the uniform assumption by up to 4.08 dB at the transmitter, and 4.11 dB at the receiver. In comparison with the unimodal assumption, the improvement is 1.63 dB at the transmitter, and 2.11 dB at the receiver. If we limit ourselves to the 95% strongest values in the angular RSC spectrum, the error between the RSC and the multimodal DMC assumption can be as low as 2.65 dB at the transmitter,

TABLE 5. Percentage of all measurement snapshots resulting in a certain number of angular DMC clusters (1, 2 or 3) at transmitter and receiver by assuming the multimodal angular DMC assumption.

Number of angular DMC clusters	Occurrence at transmitter	Occurrence at receiver
1 cluster	1.07%	0.71%
2 clusters	49.64%	61.79%
3 clusters	49.29%	37.50%

TABLE 6. Relative powers of the k-means SMC clusters and the angular DMC clusters of each von-Mises distribution.

Number of angular DMC clusters		Power at transmitter		Power at receiver	
		SMC	DMC	SMC	DMC
2 clusters	1st cluster	93%	56%	86%	56%
	2nd cluster	7%	44%	14%	44%
3 clusters	1st cluster	87%	48%	80%	49%
	2nd cluster	10%	34%	14%	34%
	3rd cluster	3%	18%	6%	17%

and 2.49 dB at the receiver. From these figures and this table, we can conclude that the multimodal angular DMC distribution fits the RSC spectrum better than when we apply a uniform- or a unimodal angular DMC assumption.

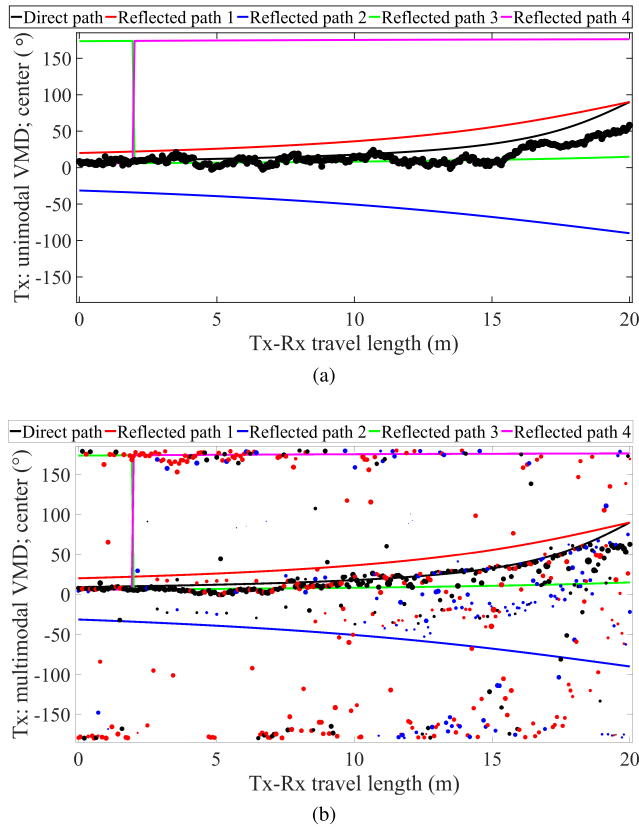
### C. NUMBER OF ANGULAR DMC CLUSTERS AND THEIR POWERS

Table 5 lists how many clusters are estimated (i.e., how many modes exist in the multimodal von-Mises distribution) when evaluating the multimodal DMC assumption.

From Table 5, we can conclude that in the angular RSC spectrum at the transmitter, a total of 2 clusters are modeled in the multimodal DMC assumption in around 50% of all cases (out of all measured snapshots). In the angular RSC spectrum at the receiver, a total of 2 clusters are modeled in around 62% of all cases. A total of 3 clusters are modeled at the transmitter in around 49% of all cases, whilst this is only 38% at the receiver. From this, we can conclude that the angular RSC spectrum at transmitter contains, on average, more clusters in our measurement scenario. This can be explained by the fact that the receiver is located near a wall, resulting in two relatively stronger clusters (direct path+ reflection on the wall).

Table 6 lists the relative power of each cluster of the k-means clustered SMC, and the angular DMC clusters of each von-Mises distribution, for when 2 or 3 clusters are estimated.

From Table 6, we can conclude that the power of the SMC is often concentrated in the strongest cluster, which contains a larger percentage of the total power on average, often with values around 80% or more. Looking at the relative percentage of the power in each angular DMC cluster, we can state that these clusters are power-wise less concentrated than their SMC counterparts. This means that the diffuse power in



**FIGURE 6.** Center values of the von Mises distributions at transmitter. (a) Unimodal assumption. (b) Multimodal assumption.

the angular RSC spectrum is distributed more equally over different clusters, especially over the two strongest clusters.

**D. CENTER VALUES OF THE VON MISES DISTRIBUTIONS**

Figure 6 shows the center values  $\mu$  of the unimodal- and multimodal angular DMC distributions at the transmitter for the 280 distinct Tx-Rx positions, shown as a function of their traveled length along the measurement route (0 m to 20 m). and Figure 7 shows these center values of the unimodal- and multimodal angular DMC distributions at the receiver. In these figures, the direct path is shown in black, and the angles of the dominant reflections (on all four walls) are shown in red, blue, green and magenta. ‘Reflected path 1’ refers to a specular reflection of a path on a wall, resulting in the shortest path length between transmitter and receiver. ‘Reflected path 4’ refers to a specular reflection of a path on a wall, resulting in the longest path length between transmitter and receiver.

Figures 6b and 7b show that the center values of the multimodal DMC clusters follows those of the specularly reflected paths in the environment quite well. The black dots denote the strongest clusters, whilst the red- and blue dots denote the weaker clusters. We can state that the stronger cluster characterize the direct path between transmitter and receiver better, and the weaker clusters characterize a reflection (more specifically, the 3rd and 4th strongest) in the environment.

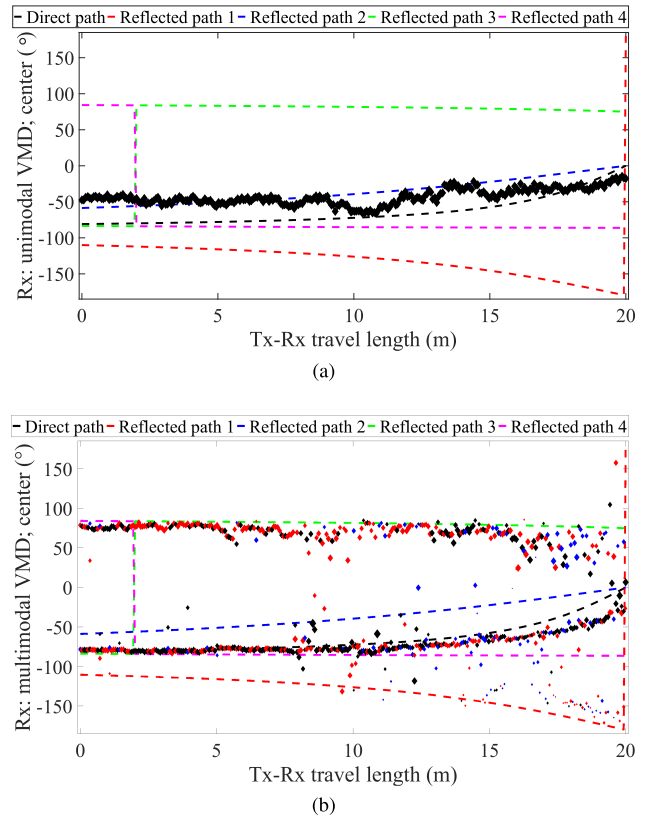


**FIGURE 7.** Center values of the von Mises distributions at receiver. (a) Unimodal assumption. (b) Multimodal assumption.

Visually, Figure 7b shows the multimodal assumption at the receiver is a better fit for the direct path than the unimodal assumption (which is shown in Figure 7a), since it follows the direct path between transmitter and receiver better.

Table 7 lists the average differences between the center values of the unimodal- and multimodal von Mises distributions with the angle of the closest (in angular space) physical path in the environment. Before performing this analysis, all 5 possible paths between transmitter and receiver were calculated, together with their corresponding AoD and AoA values. These 5 paths are the direct path and the four perfectly specular reflections in the environment (on the top wall, the bottom wall, the left wall and the right wall). The closest path was then the path corresponding with the smallest difference between each of these 5 paths and the center values of the unimodal- and multimodal von Mises distributions. The unimodal von Mises distribution results in only one such difference, whilst the multimodal von Mises distribution results in up to 3 such differences.

From Table 7, we can conclude that the angular differences between the center values of the von Mises distributions with the closest physical path in the environment increases from a difference of about 6.40° at transmitter and 8.21° at receiver when applying a unimodal DMC assumption (which only characterizes the direct path), to about 8.91° at transmitter and 10.55° at receiver when applying a multimodal DMC

**TABLE 7.** Differences of the center values  $\mu_T$  and  $\mu_R$  of the unimodal- and multimodal von Mises distributions with the AoD and the AoA of the closest physical path in the environment.

		$\mu_T$ -AoD differences	$\mu_R$ -AoA differences
DMC	unimodal	6.40°	8.21°
DMC	1st cluster	8.91°	10.55°
DMC	2nd cluster	10.64°	8.89°
DMC	3rd cluster	18.75°	12.47°

**TABLE 8.** Differences of the center values  $\mu_T$  and  $\mu_R$  of the unimodal- and multimodal von Mises distributions with the AoD and the AoA center values of the clustered SMC in the environment.

		$\mu_T$ -AoD differences	$\mu_R$ -AoA differences
DMC	unimodal	11.89°	27.83°
DMC	1st cluster	17.40°	13.49°
DMC	2nd cluster	23.66°	13.15°
DMC	3rd cluster	17.08°	15.50°

assumption (which characterizes the direct path better for Tx-Rx travel lengths up to 13 m, and also characterizes a reflection in the environment). Moreover, we can observe that the weaker clusters of the multimodal von Mises distribution characterizes reflected paths in the environment, with a difference of about 10.64° at transmitter, and 8.89° at receiver for the 2nd strongest cluster, and 18.75° at transmitter, and 12.47° at receiver for the weakest cluster. These differences indicate a strong correlation between the center values of the multimodal von Mises distributions with the expected propagation phenomena (direct path and reflections) in the environment.

Table 8 lists the average differences between the center values  $\mu_T$  and  $\mu_R$  of the unimodal- and multimodal von Mises distributions with the center values of the clustered SMC in the environment, in angular space. The SMC were clustered using the k-means algorithm, using the same number of clusters as there are in the multimodal von Mises distribution at transmitter and receiver.

Figure 8 shows the map of the environment with the center values of the multimodal von Mises distributions at transmitter and receiver. The green lines denote the center values of the multimodal distributions at the transmitter, whilst the magenta lines denote the center values of the multimodal distributions at the receiver.

Figure 8 shows that especially at the receiver, the center values of the multimodal von Mises distributions characterize both the direct path between transmitter and receiver, and the reflection on the left wall. This leads us to believe that in this measurement environment, the multimodal von Mises distributions characterizes the diffuse scattering which is linked

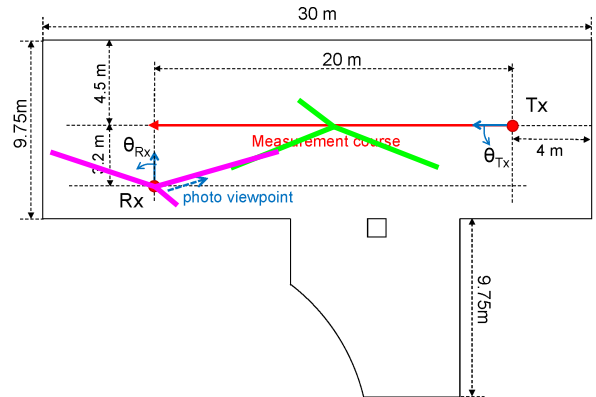


**FIGURE 8.** Map of the environment with the center values of the multimodal von Mises distributions at transmitter and receiver for snapshot 140.

with a physical reflection in the environment. This observation is in agreement with the findings in [22] and [23], who both model the DMC as clusters around the most dominant SMC in the environment.

**E. ANGULAR SPREADS OF THE VON MISES DISTRIBUTIONS**

Figure 9a shows the angular spreads  $\kappa$  (converted to °) of the SMC clusters, and the unimodal- and multimodal von Mises distributions at the transmitter, and Figure 9b shows these at the receiver. The sizes of the dots represents the relative power of the SMC- or the multimodal clusters. Obviously, there is only one dot for the unimodal distribution, which contains only a single cluster.

Figure 9a shows that the angular spread of the stronger cluster of the multimodal von Mises distribution at the transmitter and receiver (larger dots) is lower than the angular spread of the single cluster of the unimodal von Mises distribution. This finding is in agreement with our previous work on synthetic radio channels, where we found that a multimodal DMC assumption models the angular spreads of an RSC spectrum better than a unimodal assumption [28]. Moreover, Figure 9a shows that roughly 95% of all multimodal von Mises distributions result in a lower angular spread than the unimodal von Mises distribution, of which the stronger cluster follows the angular spread of the SMC.

Table 9 lists the average angular spreads of the SMC, and of the unimodal- and multimodal von Mises distributions in the environment.

Table 9 shows that the angular spread of the SMC is lower than those of the unimodal- and multimodal von Mises distributions, both at the transmitter and receiver. The average value of the angular spread of the SMC at the transmitter is 11.65° for the stronger cluster, and increases up to 16.60° for the weaker cluster. At the receiver, the angular spread is 15.78° for the stronger cluster, and 15.11° for the weaker cluster. The angular spreads of the unimodal von Mises distributions are 77.59° at the transmitter and 83.73° at the

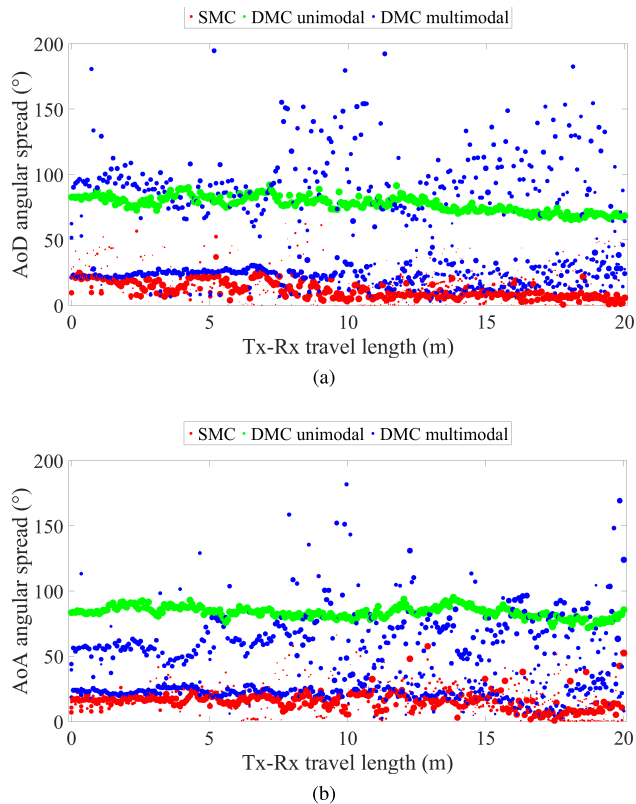


FIGURE 9. Angular spreads of the SMC clusters, and the unimodal- and multimodal von Mises distributions. The sizes of the dots represents the relative powers of the different clusters. (a) Transmitter. (b) Receiver.

TABLE 9. Average values of the angular spreads of the SMC, and of the unimodal- and multimodal von Mises distributions ( $\kappa_T$  and  $\kappa_R$ ) in the environment.

		Angular spread at transmitter	Angular spread at receiver
SMC	1st cluster	11.65°	15.78°
	2nd cluster	16.66°	18.64°
	3rd cluster	16.60°	15.11°
DMC unimodal		77.59°	83.73°
DMC multimodal	1st cluster	36.65°	40.90°
	2nd cluster	69.13°	48.41°
	3rd cluster	46.96°	39.68°

receiver, which are higher values than the ones reported for the SMC. Finally, for the multimodal von Mises distributions, we can observe that the angular spreads of the stronger cluster lie somewhere between those of the angular spreads of the SMC, and those of the unimodal von Mises distributions. The average value of the angular spread of the multimodal von Mises distribution at the transmitter is 36.65° for the stronger cluster (87% of all measured positions), and increases up to 46.96° for the weaker cluster (3% of all measured positions). At the receiver, the angular spread is 40.90° for the stronger

TABLE 10. Required number of eigenvalues to reconstruct 90%, 95% and 99% of the power in the covariance matrix  $R(\theta_d)$  of the measured radio channel.

		Power to reconstruct in $R(\theta_d)$		
		90%	95%	99%
Required nr. of eigenvalues	mean	2.66	3.47	6.38
	stdvar	0.98	1.40	2.06

cluster (49% of all measured positions), and 39.68° for the weaker cluster (17% of all measured positions).

We can conclude that the stronger cluster is more compact than the other clusters, both for the SMC and the multimodal von Mises distributions. By analyzing the center values of the SMC and of the multimodal von Mises distributions, we know that this stronger cluster characterizes the direct path between transmitter and receiver. It can be expected that this power is more concentrated in angular space. In contrast, we know that the weaker cluster of the SMC and of the multimodal von Mises distributions characterizes a reflection in the environment. The increase in angular spread for this weaker cluster implies that the diffuse scattering occurs at a wider range of angles in the environment.

F. RECONSTRUCTION OF EIGENVALUES

To evaluate the accuracy of the reconstruction of the measured eigenvalues with the multimodal approach, we will first look into how many eigenvalues are to be considered relevant to do so. We define the  $k^{th}$  relative eigenvalue as follows:

$$\lambda_{k,rel} = \frac{\lambda_k}{\sum_{n=1}^N \lambda_n}, \tag{43}$$

in which the relative eigenvalues are normalized with respect to the sum of all eigenvalues of the covariance matrix of the measured channel. This means that each relative eigenvalue can be interpreted as a fraction of the total measured power in the radio channel. Whilst most studies such as [26], [31], and [43] will only look at the four strongest eigenvalues, we have first calculated the number of eigenvalues that are required to reconstruct 90%, 95% and 99% of the power in the covariance matrix of the measured channel. The results of this can be found in Table 10.

Table 10 shows that we can reconstruct 90% of the power in the covariance matrix of the measured channel with a mean number of 2.66 eigenvalues, 95% can be reconstructed with a mean number of 3.47 eigenvalues, and 99% can be reconstructed with a mean number of 6.38 eigenvalues. Note that our measurement scenario results in a total of 24 eigenvalues. If we would only consider the 4 strongest eigenvalues, we could still underestimate the MIMO transmission performance by up to 10%. On average, we can state that we can reconstruct 99% of the power with the strongest 7 eigenvalues.

**TABLE 11. Differences between the power of the eigenvalues of the total measured covariance matrix, and the eigenvalues of the total reconstructed covariance matrix, either from the SMC, SMC+DMC (uniform), SMC+DMC (unimodal) or SMC+DMC (multimodal).**

Eigenvalue	SMC	SMC+DMC (uniform)	SMC+DMC (unimodal)	SMC+DMC (multimodal)
1 st	-1.42 dB	-0.95 dB	-0.80 dB	-0.71 dB
2 nd	-2.08 dB	-1.50 dB	-1.34 dB	-1.22 dB
3 rd	-3.59 dB	-1.30 dB	-1.29 dB	-1.05 dB
4 th	-4.38 dB	-1.54 dB	-1.26 dB	-0.93 dB
5 th	-5.27 dB	-0.79 dB	-0.57 dB	-0.37 dB
6 th	-5.55 dB	-0.70 dB	-0.92 dB	-0.31 dB
7 th	-7.30 dB	-1.06 dB	-0.91 dB	-0.37 dB

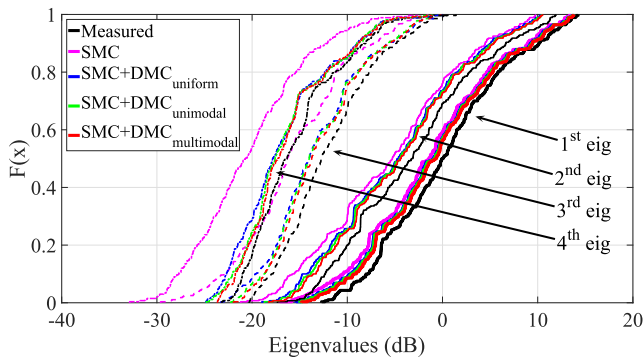


**FIGURE 10. Eigenvalues CDFs of space MIMO matrices of the total channel.**

Table 11 lists the differences between the power of the eigenvalues of the total measured covariance matrix, with the eigenvalues of the total covariance matrix reconstructed based on either the SMC, the SMC and a unimodal DMC assumption, or the SMC and a multimodal DMC assumption, and this for the strongest seven eigenvalues.

From Table 11, we can state that we are able to reconstruct the measured channel better with a multimodal assumption than with a uniform- or a unimodal assumption, since all eigenvalues lie consistently closer to the measured ones. Although the improvement of our approach over the uniform- and the unimodal assumption are less than 1 dB by considering the eigenvalues, it results in a more accurate reconstruction of the angular RSC spectrum. Figure 10 shows the CDFs for the four strongest eigenvalues (we have limited this figure to the strongest four, for visual purposes).

Figure 10 shows a modest improvement for the reconstruction of the eigenvalues when applying a multimodal angular DMC assumption over a unimodal- or a uniform angular DMC assumption. However, from Figure 5, we know that the uniform- or the unimodal angular DMC assumption will add extra power to the reconstructed channel, which helps the reconstruction of the eigenvalues, but at the cost of ignoring the underlying structure of the angular RSC spectrum.

**VII. CONCLUSIONS**

In this chapter, we have performed a channel sounding measurement campaign at 11 GHz in an indoor environment.

We have analyzed the Power Angular Profile (PAP) of the Residual Signal Components (RSC), which can be obtained after removal of the SMC from the measured radio channel, by estimating them with the SAGE algorithm. We found that the RSC in the angular domain should be modeled by taking into account multiple angular clusters, to better characterize the diffuse scattering between transmitter and receiver, originating from multiple reflections which occur in an indoor hall environment. The RSC is assumed to largely consist of contributions by Dense Multipath Components (DMC), originating from distributed diffuse scattering of the electromagnetic waves on rough surfaces. Therefore, we proposed to extend the ML estimation of the DMC parameters in the RiMAX algorithm from a unimodal to a multimodal assumption in the angular domain. By doing so, we are able to model the angular spectrum of the RSC by a multimodal von Mises distribution (a combination of several von Mises distributions), to account for multiple clusters in this spectrum. This allows us to better characterize the diffuse scattering between transmitter and receiver, originating from multiple reflections in an environment.

We have applied our proposed method to the measured data, which indicate that our approach leads to a better characterization of the underlying structure of the angular spectrum of the RSC. By applying our proposed method to reconstruct this spectrum, we are able to reduce the Mean-Square-Error (MSE) at the transmitter from about 7.65 dB with a uniform assumption to 5.20 dB with a unimodal assumption, down to 3.57 dB with a multimodal assumption. At the receiver, the MSE of our method with the RSC reduces from 7.49 dB with a uniform assumption to 5.49 dB with a unimodal assumption, down to 3.38 dB with a multimodal assumption. From this analysis, we can conclude that the multimodal angular DMC assumption fits the RSC spectrum better than when we would apply a uniform- or a unimodal assumption. We have also found a correlation between the location of the angular DMC clusters with the physical propagation paths in the environment. Moreover, we have found that the multimodal DMC assumption results in more compact angular DMC clusters with a lower angular spread than when we would apply a unimodal DMC assumption. We have also shown that our approach is able to distinguish better between the shadowed and the radiated regions in the RSC, of which the multimodal DMC assumption characterizes the highs and lows of the RSC spectrum better than the unimodal DMC assumption.

We have also shown that our approach leads to a consistently better reconstruction of the eigenvalues of the measured channel for this measurement scenario, and thus of the total power in the channel. Since this is of importance to accurately characterize the true Multiple-Input Multiple-Output (MIMO) transmission performance, and to assess the channel capacity of wireless communication systems, this highlights the necessity of taking into account a multimodal DMC assumption over a unimodal one. Although the obtained improvements of our multimodal DMC assumption are

modest when considering the reconstruction of the eigenvalues, we know that the improvements of assuming of uniform- or a unimodal DMC assumption are flawed when looking at their reconstructed angular DMC spectra. By analyzing these spectra, we know that they either average the entire spectrum with a uniform assumption, or result in faulty estimates of their center locations and angular spreads with a unimodal assumption.

## REFERENCES

- [1] T. S. Rappaport *et al.*, “Millimeter wave mobile communications for 5G cellular: It will work!” *IEEE Access*, vol. 1, pp. 335–349, 2013.
- [2] K. Sakaguchi *et al.*, “Millimeter-wave wireless LAN and its extension toward 5G heterogeneous networks,” *IEICE Trans. Commun.*, vol. E98-B, no. 10, pp. 1932–1948, 2010.
- [3] P. Beckmann and A. Spizzichino, *The Scattering of Electromagnetic Waves From Rough Surfaces* (Artech House Radar Library). Norwood, MA, USA: Artech House, 1987.
- [4] N. Czink, A. Richter, E. Bonek, J.-P. Nuutinen, and J. Ylitalo, “Including diffuse multipath parameters in MIMO channel models,” in *Proc. IEEE Veh. Technol. Conf. (VTC)*, Sep./Oct. 2007, pp. 874–878.
- [5] A. Richter, J. Salmi, and V. Koivunen, “Distributed scattering in radio channels and its contribution to MIMO channel capacity,” in *Proc. Eur. Space Agency, (Special Publication) ESA SP*, vol. 626, 2006, pp. 1–7.
- [6] *Spacial Channel Model for Multiple Input Multiple Output (MIMO) Simulations*, 3GPP, Sophia Antipolis Cedex, France, 2016.
- [7] W. C. Emmens, “Introduction and scope,” in *Formability* (Springer Briefs in Applied Sciences and Technology). Berlin, Germany: Springer, 2011.
- [8] J. Meinilä, P. Kyösti, T. Jämsä, and L. Hentilä, “WINNER II channel models,” in *Radio Technologies and Concepts for IMT-Advanced*, vols. 1–2, 2010, pp. 39–92.
- [9] V. Degli-Esposti, F. Fuschini, E. M. Vitucci, and G. Falciasecca, “Measurement and modelling of scattering from buildings,” *IEEE Trans. Antennas Propag.*, vol. 55, no. 1, pp. 143–153, Jan. 2007.
- [10] Y. Lostanlen and G. Gougeon, “Introduction of diffuse scattering to enhance ray-tracing methods for the analysis of deterministic indoor UWB radio channels (Invited Paper),” in *Proc. Int. Conf. Electromagn. Adv. Appl. (ICEAA)*, Sep. 2007, pp. 903–906.
- [11] E. M. Vitucci, F. Mani, V. Degli-Esposti, and C. Oestges, “A study on polarimetric properties of scattering from building walls,” in *Proc. IEEE Veh. Technol. Conf. (VTC)*, Sep. 2010, pp. 1–5.
- [12] F. Mani, F. Quitin, and C. Oestges, “Directional spreads of dense multipath components in indoor environments: Experimental validation of a ray-tracing approach,” *IEEE Trans. Antennas Propag.*, vol. 60, no. 7, pp. 3389–3396, Jul. 2012.
- [13] E. M. Vitucci, F. Mani, V. Degli-Esposti, and C. Oestges, “Polarimetric properties of diffuse scattering from building walls: Experimental parameterization of a ray-tracing model,” *IEEE Trans. Antennas Propag.*, vol. 60, no. 6, pp. 2961–2969, Jun. 2012.
- [14] A. Bamba *et al.*, “Experimental investigation of electromagnetic reverberation characteristics as a function of UWB frequencies,” *IEEE Antennas Wireless Propag. Lett.*, vol. 14, pp. 859–862, 2015.
- [15] A. Richter, “Estimation of radio channel parameters: Models and algorithms,” Ph.D. dissertation, Fakultät Elektrotech. Informationstech., Tech. Univ. Ilmenau, Ilmenau, Germany, 2005.
- [16] A. Richter and R. S. Thomä, “Joint maximum likelihood estimation of specular paths and distributed diffuse scattering,” in *Proc. IEEE Veh. Technol. Conf. (VTC)*, vol. 1, May/June 2005, pp. 11–15.
- [17] A. Richter, J. Salmi, and V. Koivunen, “An algorithm for estimation and tracking of distributed diffuse scattering in mobile radio channels,” in *Proc. IEEE Workshop Signal Process. Adv. Wireless Commun.*, Jul. 2006, pp. 1–5.
- [18] B. Hanssens *et al.*, “An extension of the RiMAX multipath estimation algorithm for ultra-wideband channel modeling,” *EURASIP J. Wireless Commun. Netw.*, vol. 2018, Dec. 2018, Art. no. 164.
- [19] E. Tanghe, D. P. Gaillot, M. Liénard, L. Martens, and W. Joseph, “Experimental analysis of dense multipath components in an industrial environment,” *IEEE Trans. Antennas Propag.*, vol. 62, no. 7, pp. 3797–3805, Jul. 2014.
- [20] D. P. Gaillot *et al.*, “Polarization properties of specular and dense multipath components in a large industrial Hall,” *IEEE Trans. Antennas Propag.*, vol. 63, no. 7, pp. 3219–3228, Jul. 2015.
- [21] M. Landmann, K. Sivasondivat, J.-I. Takada, I. Ida, and R. Thomä, “Polarization behavior of discrete multipath and diffuse scattering in urban environments at 4.5 GHz,” *EURASIP J. Wireless Commun. Netw.*, vol. 2007, Dec. 2007, Art. no. 057980.
- [22] J. Poutanen, J. Salmi, K. Haneda, V. M. Kolmonen, F. Tufvesson, and P. Vainikainen, “Propagation characteristics of dense multipath components,” *IEEE Antennas Wireless Propag. Lett.*, vol. 9, pp. 791–794, 2010.
- [23] F. Quitin, C. Oestges, F. Horlin, and P. De Doncker, “Diffuse multipath component characterization for indoor MIMO channels,” in *Proc. Eur. Conf. Antennas Propag. (EuCAP)*, Apr. 2010, pp. 1–5.
- [24] C. B. Ribeiro, A. Richter, and V. Koivunen, “Joint angular- and delay-domain MIMO propagation parameter estimation using approximate ML method,” *IEEE Trans. Signal Process.*, vol. 55, no. 10, pp. 4775–4790, Oct. 2007.
- [25] M. Käske and R. Thomä, “Maximum-likelihood based estimation of angular parameters of dense-multipath-components,” in *Proc. Eur. Conf. Antennas Propag. (EuCAP)*, Apr. 2015, pp. 1–6.
- [26] K. Saito, J.-I. Takada, and M. Kim, “Dense multipath component characteristics in 11-GHz-band indoor environments,” *IEEE Trans. Antennas Propag.*, vol. 65, pp. 4780–4789, Sep. 2017.
- [27] K. Saito, J.-I. Takada, and M. Kim, “Dense multipath component parameter estimation in 11 GHz-band indoor environment,” in *Proc. IEEE 27th Annu. Int. Symp. Pers., Indoor, Mobile Radio Commun. (PIMRC)*, Sep. 2016, pp. 1–6.
- [28] B. Hanssens *et al.*, “Modeling the power angular profile of dense multipath components using multiple clusters,” in *Proc. Eur. Conf. Antennas Propag. (EuCAP)*, London, U.K., 2018, pp. 1–5.
- [29] M. Kim, Y. Konishi, Y. Chang, and J.-I. Takada, “Large scale parameters and double-directional characterization of indoor wideband radio multipath channels at 11 GHz,” *IEEE Trans. Antennas Propag.*, vol. 62, no. 1, pp. 430–441, Jan. 2014.
- [30] K. Saito, J. I. Takada, and M. Kim, “Dense multipath component characteristics in 11 GHz-band indoor environments,” in *Proc. 2nd Tech. Meeting COST Action CA, IRACON*, Durham, U.K., 2016, pp. 1–11.
- [31] U. T. Virk, K. Haneda, and J.-F. Wagen, “Dense multipath components add-on for COST 2100 channel model,” in *Proc. Eur. Conf. Antennas Propag. (EuCAP)*, Apr. 2015, pp. 1–5.
- [32] R. S. Thomä, M. Landmann, G. Sommerkorn, and A. Richter, “Multidimensional high-resolution channel sounding in mobile radio,” in *Proc. Instrum. Meas. Technol. Conf. (IMTC)*, vol. 1, May 2004, pp. 257–262.
- [33] C. B. Ribeiro, A. Richter, and V. Koivunen, “Stochastic maximum likelihood estimation of angle- and delay-domain propagation parameters,” in *Proc. IEEE 16th Int. Symp. Pers., Indoor Mobile Radio Commun. (PIMRC)*, vol. 1, Sep. 2005, pp. 624–628.
- [34] J. Salmi *et al.*, “Incorporating diffuse scattering in geometry-based stochastic MIMO channel models,” in *Proc. Eur. Conf. Antennas Propag. (EuCAP)*, Apr. 2010, pp. 1–5.
- [35] J. A. Fessler and A. O. Hero, “Space-alternating generalized expectation-maximization algorithm,” *IEEE Trans. Signal Process.*, vol. 42, no. 10, pp. 2664–2677, Oct. 1994.
- [36] E. W. Forgy, “Cluster analysis of multivariate data: Efficiency versus interpretability of classification,” *Biometrics*, vol. 21, no. 3, pp. 768–769, 1965.
- [37] *COST 273 Action. No Title*. [Online]. Available: <http://www.lx.it.pt/cost273>
- [38] *COST 2100 Action. No Title*. [Online]. Available: [http://www.cost.eu/COST\\_Actions/ict/2100](http://www.cost.eu/COST_Actions/ict/2100)
- [39] D.-J. Kim, Y.-W. Park, and D.-J. Park, “A novel validity index for determination of the optimal number of clusters,” *IEICE Trans. Inf. Syst.*, vol. E84-D, no. 2, pp. 281–285, 2001.
- [40] T. W. Anderson, “Estimation of covariance matrices which are linear combinations or whose inverses are linear combinations of given matrices,” in *Essays in Probability and Statistics*. Chapel Hill, NC, USA: Univ. of North Carolina Press, 1970.
- [41] R. Waagepetersen. (Aug. 2012). “Maximum likelihood estimation for linear mixed models.” [Online]. Available: <http://people.math.aau.dk/~rw/Undervisning/Mat6F12/Handouts/2.hand.pdf>

- [42] J. Salmi, A. Richter, and V. Koivunen, "Detection and tracking of MIMO propagation path parameters using state-space approach," *IEEE Trans. Signal Process.*, vol. 57, no. 4, pp. 1538–1550, Apr. 2009.
- [43] C. Gustafson, K. Haneda, S. Wyne, and F. Tufvesson, "On mm-wave multipath clustering and channel modeling," *IEEE Trans. Antennas Propag.*, vol. 62, no. 3, pp. 1445–1455, Mar. 2014.



**BRECHT HANSSENS** was born in Ghent, Belgium, in 1989. He received the M.Eng. degree in electronics and ICT engineering with electronics as his main subject from the Catholic University of Leuven (KU Leuven) in 2011 and the M.Sc. degree in electrical engineering with ICT as his main subject and the Ph.D. degree in electrical engineering from Ghent University in 2013 and 2018, respectively. He is currently a member of the WAVES Group, Department of Information

Technology, INTEC, Ghent University. His current research interests include ultra-wideband communication, channel modeling for specular and dense multipath components, modeling the angular spectrum of radio channel data, localization techniques based on multipath parameters, and parameter estimation frameworks.



**KENTARO SAITO** (M'17) was born in Kanagawa, Japan, in 1977. He received the B.S. and Ph.D. degrees from The University of Tokyo, Tokyo, Japan, in 2002 and 2008, respectively. In 2002, he joined NTT DOCOMO, Japan, where he has been involved in the research and development of mobile communication systems and radio propagation. In 2015, he joined the Tokyo Institute of Technology, Tokyo, where he has been involved in research on radio propagation for mobile communication systems. He is a Senior Member of IEICE.



**EMMERIC TANGHE** (M'14) was born in Tielt, Belgium, in 1982. He received the M.Sc. and Ph.D. degrees in electrical engineering from Ghent University, Ghent, Belgium, in 2005 and 2011, respectively. From 2005 to 2011, he was a Research Assistant with the Department of Information Technology, imec-UGent/INTEC, Ghent University. His scientific work focused on the modeling of indoor and outdoor propagation through field measurements. Since 2011, he has been a Post-

Doctoral Researcher with Ghent University and continues his work in propagation modeling. Since 2012, he has been a Post-Doctoral Fellow with the Research Foundation Flanders. In 2015, he became a part-time professor of medical applications of electromagnetic fields in and around the human body.



**LUC MARTENS** (M'92) received the M.Sc. degree in electrical engineering from Ghent University, Ghent, Belgium, in 1986, and the Ph.D. degree in 1990. From 1986 to 1990, he was a Research Assistant with the Department of Information Technology, INTEC, Ghent University. During this period, his scientific work focused on the physical aspects of hyperthermic cancer therapy. His research work dealt with electromagnetic and thermal modeling and the development of measurement systems for that application. Since 1991, he has been managing the WAVES Research Group (Wireless and Cable Research Group), INTEC. This group has been a part of the imec Institute since 2004. Since 1993, he has been a Professor with Ghent University. He has authored/co-authored over 300 publications in the domain of electromagnetic channel predictions, dosimetry, exposure systems and health, and wireless communications. His research interests include modeling and measurement of electromagnetic channels, in electromagnetic exposure, e.g., around telecommunication networks and systems, such as cellular base station antennas, and in energy consumption of wireless networks.



**WOUT JOSEPH** (M'05–SM'12) was born in Ostend, Belgium, in 1977. He received the M.Sc. and Ph.D. degrees in electrical engineering from Ghent University, Ghent, Belgium, in 2000 and 2005, respectively. From 2000 to 2005, he was a Research Assistant with the Department of Information Technology, INTEC, Ghent University. During this period, his scientific work focused on electromagnetic exposure assessment. Since 2005, he has been a Post-Doctoral Researcher with imec-UGent/INTEC. From 2007 to 2013, he was a Post-Doctoral Fellow with the Research Foundation Flanders. Since 2009, he has been a professor of the domain of experimental characterization of wireless communication systems. His research interests include measuring and modeling electromagnetic fields around base stations for mobile communications, health effects of exposure to electromagnetic radiation, electromagnetic exposure assessment, propagation for wireless communication systems, and antennas and calibration. He also specializes in wireless performance analysis and quality of experience.



**JUN-ICHI TAKADA** (S'89–M'93–SM'11) received the B.E., M.E., and D.E. degrees in electrical and electronics engineering from the Tokyo Institute of Technology, Tokyo, Japan, in 1987, 1989, and 1992, respectively. He was a Research Associate with Chiba University, Chiba, Japan, from 1992 to 1994, and an Associate Professor with the Tokyo Institute of Technology from 1994 to 2006. Since 2006, he has been a Professor with the Tokyo Institute of Technology. He was a Researcher with the National Institute of Information and Communications Technology, Japan, from 2003 to 2007. His research interests include radio-wave propagation and channel modeling for mobile and short-range wireless systems, regulatory issues of spectrum sharing, and ICT applications for international development. He is a fellow of IEICE, Japan.

...